Aortic Flow Patterns before and after Personalised External Aortic Root Support Implantation in Marfan Patients

S. D. Singh[a], X. Y. Xu[a,*], N. B. Wood[a], J. R. Pepper[b,c], C. Izgi[b], T. Treasure[d], R. H. Mohiaddin[b,c]

[a]Department of Chemical Engineering, Imperial College London, South Kensington Campus, London SW7 2AZ, UK

[b]Royal Brompton and Harefield NHS Foundation Trust, Sydney Street, London SW3 6NP, UK

[c]National Heart and Lung Institute, Imperial College London, London SW7 2AZ, UK

[d]Clinical Operational Research, University College London, Department of Mathematics, 4 Taviton Street, London WC1H 0BT, UK

* Corresponding author. Tel.: +44 (0)2075945588; Fax: +44 (0)2075941989; E-mail: yun.xu@imperial.ac.uk

Word count: 4843 (excluding references)

ABSTRACT

Implantation of a personalised external aortic root support (PEARS) in the Marfan aorta is a new procedure that has emerged recently, but its haemodynamic implication has not been investigated. The objective of this study was to compare the flow characteristics and hemodynamic indices in the aorta before and after insertion of PEARS, using combined cardiovascular magnetic resonance imaging (CMR) and computational fluid dynamics (CFD). Pre- and post-PEARS MR images were acquired from 3 patients and used to build patient-specific models and upstream flow conditions, which were incorporated into the CFD simulations. The results revealed that while the qualitative patterns of the haemodynamics were similar before and after PEARS implantation, the post-PEARS aortas had slightly less disturbed flow at the sinuses, as a result of reduced diameters in the post-PEARS aortic roots. Quantitative differences were observed between the pre- and post-PEARS aortas, in that the mean values of helicity flow index (HFI) varied by -10%, 35% and 20% in post-PEARS aortas of Patients 1, 2 and 3, respectively, but all values were within the range reported for normal aortas. Comparisons with MR measured velocities in the descending aorta of Patient 2 demonstrated that the computational models were able to reproduce the important flow features observed in vivo.

Keywords: Personalised external aortic root support (PEARS), computational fluid dynamics (CFD), wall shear stress (WSS), helicity flow index (HFI), Marfan syndrome

1 Introduction

Marfan syndrome (MFS) is a connective tissue disorder which affects the cardiovascular, ocular and skeletal systems (Judge and Dietz, 2005). The development of thoracic aortic aneurysms is the leading cause of death in patients with MFS (Silverman et al., 1995). Treatment consists of regular imaging to determine the progression of aortic dilatation and preventative techniques include total root replacement (TRR), valve sparing root replacements (VSRR) and most recently, the insertion of a personalised external aortic root support (PEARS). In TRR, the aortic root and ascending aorta are replaced using a conduit of woven Dacron incorporating a mechanical valve, with the coronary ostia anastomosed to the tube graft (Bentall and De Bono, 1968). It has been revised both with respect to the surgical technique and the materials used. VSRR also involves radical excision of the diseased aortic root and ascending aorta, however retains the native valve leaflets (David et al., 1995, Yacoub et al., 1998). PEARS refers to a customised device described and introduced by Golesworthy et al. (2004). The insertion of PEARS is a less invasive procedure that conserves the valve and blood/endothelium interface (Pepper et al., 2010, Treasure et al., 2014). Aortic cross-sectional images of the patient are used to create a 3D replica of the aorta via rapid prototyping, on which a medical grade polymer mesh is fitted (Fig. 1). At surgery, the support is placed around the aorta, extending from the aortoventricular junction to just beyond the brachiocephalic artery. Unlike the vascular grafts used in root replacement, the fabric of PEARS becomes incorporated into the vessel wall, creating a composite aortic wall which prevents the ascending aorta from further dilatation (Verbrugghe et al., 2013, Pepper et al., 2014). PEARS is fundamentally different to the Florida sleeve in which an off-the-shelf device made of rigid graft material is placed around the root (Hess et al., 2005).

Due to their sophisticated functions, morphological changes of the aortic root and valve can influence haemodynamics in different parts of the aorta, coronary circulation and systemic circulation. While PEARS theoretically allows the natural expansion and recoil of the root and ascending aorta, its haemodynamic influence has not been investigated. Moreover, current knowledge of detailed blood flow patterns in the Marfan aorta is limited. Using flow-sensitive 4D MRI, it has been shown that helical flow is enhanced and systolic wall shear stress (WSS) increased in the Marfan aorta compared to normals (Geiger et al., 2012, 2013). There is evidence that disordered flow causes changes in local WSS (Hope et al., 2010, Lorenz et al., 2014); and WSS in turn alters endothelial cell function and results in arterial remodelling, linked to the development of autophagy such as dilatation or aneurysms (Malek et al., 1999). One of the concerns associated with PEARS is that increased stiffness of the supported aorta will affect the working load of the heart, blood flow patterns and consequently WSS. Furthermore, the aorta distal to the support is unprotected and vulnerable to dilatation, which is of course a limitation more obviously consequences of TRR, VSRR and the Florida sleeve (Treasure et al., 2014).

Numerical simulations combining cardiovascular magnetic resonance (CMR) imaging and computational fluid dynamics (CFD) are commonly used for detailed aortic flow analysis. Blood flow in the aorta is complex and may involve transition from a well-organised laminar regime to a chaotic turbulent regime, under both normal and pathological conditions (Stein and Sabbah, 1976, Stalder et al., 2011). In an attempt to capture laminar-turbulent transition, CFD studies have employed different simulation methods including direct numerical simulation (DNS), large eddy simulation (LES) and turbulence models based on Reynolds-averaged Navier-Stokes (RANS). DNS is considered the gold standard as it provides numerical solutions of the Navier-Stokes equation by resolving all spatial and temporal scales.

Due to high computational costs associated with DNS, LES and RANS-based turbulence models have been tested as potential alternatives for aortic flow modelling. In LES, large turbulent eddies are resolved and smaller ones are modelled, while in RANS methods, the effect of turbulent fluctuations on mean flow is accounted for via different turbulence models. Mittal et al. (2003) and Paul et al. (2009) employed LES for flow in aortic coarctation while Lantz et al. (2012, 2013) used LES for patient-specific models of the aorta and aortic coarctation. However, no direct comparison of DNS and LES for aortic flow has been found in the literature.

On the other hand, transitional and turbulent flow in arterial stenosis has been studied more extensively. Varghese et al. (2007a, 2007b) performed DNS of steady and pulsatile flows through idealised stenoses, and compared DNS results with LES and RANS-based models (Varghese et al., 2008). Tan et al. (2011) also compared the DNS results of Varghese et al. (2008) with LES and RANS models involving a correlation-based transitional version of the hybrid k-ε/k-ω model, and experimental data (Ahmed and Giddens, 1983a, 1983b). Their study revealed that both dynamic Smagorinsky LES and the RANS transitional model captured the complex transition phenomena under physiological Reynolds numbers and predicted comparable velocity and turbulence intensity profiles (Tan et al., 2011). The RANS transitional model was also found to perform better than the other RANS turbulence models tested for flow in an axisymmetric stenosis (Tan et al., 2008). Positive experience with the RANS transition model was also reported for flow in patient-specific thoracic aortic aneurysms (Tan et al., 2009a, 2009b, Lantz et al., 2011) demonstrating good agreement with *in vivo* MRI data (Tan et al., 2009b).

In this study, CMR and CFD are applied to Marfan aortas in order to understand the haemodynamics associated with this disease, as well as to investigate the implications associated with PEARS implantation. Pre- and post-operative geometries for three Marfan patients were reconstructed using MR images, and physiologically realistic inflow and boundary conditions were imposed. Blood flow patterns, helicity flow indices and WSS in the pre- and post-PEARS aortas were compared.

2 Methods

2.1 MR imaging

Electrocardiographic-gated MR images for three patients pre- and post-PEARS were obtained using a 1.5 Tesla scanner (Avanto, Siemens, Erlangen, Germany). The images covered aortic root, ascending aorta, aortic arch and proximal descending aorta in three orthogonal planes. They were acquired in diastole, at the same point in the cardiac cycle. Phase contrast (PC) mapping with a fast gradient echo sequence was also performed to obtain pixel-based time-varying velocities from each patient at locations just above the aortic valves. Details of the patients' demographic data are given in Table 1. All patients had no significant aortic valve regurgitation. The study was approved by the local ethics committee, and complied with the Declaration of Helsinki.

2.2 Model reconstruction

The MR images were stored in DICOM format and processed using Mimics (Materialise, Louven, Belgium). The same segmentation algorithm and smoothing parameters were used for all cases, and the final reconstructions were checked by an experienced radiologist for accuracy. Fig. 2 shows the reconstructed pre- and post-PEARS geometries. The resulting STL files were exported into a mesh generation package, ANSYS ICEM CFD (ANSYS, Canonsburg, PA, USA) where the computational mesh for the fluid domain was generated using unstructured hexahedral elements.

2.3 Flow model and boundary conditions

The continuity equation and Reynolds averaged Navier-Stokes (RANS) equations were used to describe 3D incompressible flow. Based on the stability diagram for ascending aorta (Kousera et al., 2013), the flow regime was assessed using the peak Reynolds number ($\hat{Re}$) and the Womersley parameter (α). All three cases were above the threshold for laminar flow, hence the γ-Re_θ correlation-based transitional model (Langtry and Menter, 2009) with Menter's hybrid k-ϵ/k-ω Shear Stress Transport (SST-Trans) model (Menter, 1994) was adopted. Details of the SST-Trans model and justifications of using it for aortic flow have been reported previously (Tan et al., 2009a, Kousera et al., 2013).

Mesh independence tests were carried out on each geometry (details are provided in Appendix A1), upon which a mesh size consisting of 1.0×10^6 to 1.3×10^6 elements was adopted. PC-MR images were used to extract the flowrate waveforms (Fig. 2), which were imposed at the inlets of the aorta assuming a flat velocity profile. Key flow parameters for both the pre- and post-PEARS cases are summarised in Table 1. An inlet turbulence level was introduced to represent initial disturbances in the flow and allow transition to occur realistically. Turbulence intensity, Tu, is defined as the ratio of the root-mean-square of the turbulent velocity fluctuations to the mean velocity, and was set at 1.5% (Tan et al., 2009a).

In each of the brachiocephalic, left common carotid and left subclavian arteries, the outlet was extended by five lumen diameters to minimize the proximal effect of outflow boundary condition, and a total proportion of 30% aortic flow was assumed to leave via these branches. This was based on the average flow rates through the arch branches derived from PC-MR imaging of normal aortas (Cheng et al., 2015). A time-dependent pressure waveform was specified at the main outlet in the descending aorta. Since only the systolic and diastolic pressures were known for each patient, a typical pressure waveform for a healthy subject was adopted (Olufsen et al., 2000, Tan et al., 2009b) and modified using the known systolic and diastolic pressures for each patient. A phase shift of 0.1 s between the peak flow and peak pressure was set and all waveforms had a frequency of 1 Hz (Tan et al., 2009b). The arterial wall was assumed to be rigid and non-permeable where a no-slip boundary condition was applied. Blood was treated as a Newtonian fluid with a dynamic viscosity of 4.0×10^{-3} Pa·s and a density of 1044 kg/m^3.

2.4 Numerical approach

The governing equations were solved numerically using ANSYS CFX 14 (ANSYS, Canonsburg, PA, USA). A high-resolution advection scheme (Barth and Jespersen, 1989) was used for spatial discretisation of the governing equations while temporal discretisation was performed by the second order implicit backward Euler scheme (Ferziger and Peric, 2001). A uniform time-step of 0.001 s was used and three cardiac cycles were simulated for each flow model to ensure periodicity (Tan et al., 2009a). Convergence of the solution was controlled by defining a root-mean-square residual of 10^{-6}, which was satisfied after approximately 5-30 iterations at each time-step. Simulations were performed using a 16.0 GB RAM personal computer with Intel® Core™ i7-2600 3.40 GHz, running Windows 7 Enterprise.

2.5 Quantification of haemodynamic indices

Flow visualisation and quantification of the haemodynamic indices were performed using CEI EnSight (CEI Inc., Apex, NC, USA) and MATLAB (MathWorks, Natick, MA, USA).

2.5.1 Helicity

A Lagrangian-based descriptor, helicity flow index (HFI), was adopted to “measure” the helical motion based on a particle trace analysis of the flow using the local normalised helicity (LNH) as a basic quantity (Grigioni et al., 2005, Morbiducci et al., 2009, Morbiducci et al., 2011) (see Appendix A2 for details). In this study, N_p immaterial particles were released from the inlet at five different time points T_j (j = 1, …, 5) in systole. The mean value of the HFI calculated over the particle sets emitted at N_T = 5 time points was then evaluated:

$$\overline{\mathrm{HFI}} = \frac{1}{N_T}\sum_{j=1}^{N_T}\mathrm{HFI}_j \qquad\qquad 0 \le \overline{\mathrm{HFI}} \le 1$$

2.5.2 Wall shear stress

WSS refers to the tangential force exerted by the blood on the endothelial surface. Since it varies throughout the cardiac cycle, it is often analysed in terms of time-averaged wall shear stress (TAWSS). Whilst the reason for time-averaging is related to atherogenesis, which takes place over decades, for consideration of faster acting pathologies averaging the WSS temporally or spatially results in diluting the time-dependent (systolic phase) and spatial activity, which motivates the need to report on local WSS indices (Barker et al., 2010, Wendell et al., 2013). Four planes along the aorta were defined: sinotubular junction (P1), proximal aortic arch (P2), distal aortic arch (P3) and descending aorta (P4). The instantaneous WSS along the boundary of these planes were unwrapped, and mapped onto a normalised circumferential distance-time coordinate.

3 Results

3.1 Anatomical features

From the reconstructed models shown in Fig. 2, it can be seen that the aortic root was dilated in these patients. Small variations in the shape of the pre- and post-PEARS aortas of each patient were observed. Four transverse sections (P1, P2, P3 and P4) along the length of the aorta were selected to compare the pre- and post-PEARS sizes, which are summarised in Table 2. Patient 1 had a reduced diameter at P1 after PEARS implantation, but the aortic diameters were increased at other locations. Patient 2 and Patient 3 both had overall reductions in the post-PEARS diameters throughout the aorta.

3.2 Flow patterns

Fig. 2 also shows the pre- and post-PEARS flow waveforms (Fig. 2), indicating an increase in systolic flow post-PEARS, especially in Patient 1. Comparisons of key flow parameters (Table 1) showed a reduction in blood pressure and increase in cardiac output (up to 15%) after PEARS implantation in all patients. Instantaneous streamlines in the pre- and post-PEARS Marfan aortas of the three patients are presented in Fig. 3 at peak systole (T_{sys}) and mid-systolic deceleration (T_{mid}). Aortic flow patterns hardly changed after PEARS implantation except in the sinuses of Valsalva where flow was slightly less disturbed post-PEARS, as a result of reduced diameters in the aortic roots. Other than that, flow in both the pre- and post-PEARS aortas shared the common flow features as described below. At peak systole, areas of low velocities and recirculation were found in the sinuses, as expected (Bellhouse and Talbot, 1969). The velocities were then increased in regions distal to the aortic arch and into the descending aorta (DA), as a consequence of reduced diameter from the ascending to descending aorta. Local right-handed helical flows at the inner wall of the ascending aorta (AA) up to the proximal arch were observed. Additionally, left-handed helices were present on the outer wall and persisted up to mid-arch. A global left-handed helical pattern was observed in the DA. While these flow patterns are consistent with previously published findings in normal aortas (Bogren and Buonocore, 1999, Kilner et al., 1993), recirculation was exaggerated at the aortic root owing to the dilatation, also consistent with observations in dilated/aneurysmal ascending aortas (Markl et al., 2011a, 2011b). T_{mid}

was dominated by recirculating and/or bi-helical flow patterns throughout the length of the aorta, for both pre-and post-PEARS aortas, due to flow deceleration.

Fig. 4 shows helicity density isosurfaces at T_{sys} and T_{mid}. Comparisons between the pre- and post-PEARS aortas suggested similar patterns with minor quantitative differences in that areas of high helicity densities ($\left|H_k\right| \geq 200$) were reduced in Patient 1, but increased slightly in Patient 2 with no obvious changes in Patient 3. The common trend can be described as following: the aortic arch had the highest helicity densities, with both clockwise (positive H_k) and anti-clockwise helical flows (negative H_k), which is similar to findings reported in previous studies (Morbiducci et al., 2009) and can be attributed to the non-planarity of the AA. In general, T_{mid} showed reduced helicity densities compared to T_{sys}, as a result of flow deceleration. This can be described quantitatively in terms of $\overline{\mathrm{HFI}}$.

Fig. summarises the HFI values calculated over traces of particles emitted at five time points T_j and over the time intervals $T_{es} - T_j$, as well as the corresponding $\overline{\mathrm{HFI}}$ for each patient. It can be seen that PEARS implantation caused a reduction in HFI in Patient 1, with $\overline{\mathrm{HFI}}$ being reduced by 10%, but an increase in HFI in Patients 2 and 3, with $\overline{\mathrm{HFI}}$ being increased by 35% and 20%, respectively. However, despite variations between the pre- and post-PEARS aortas, the actual values obtained were within the range reported for healthy aortas (Morbiducci et al., 2009, Morbiducci et al., 2011).

In order to assess the validity of the simulation results, MR velocity images acquired at an additional plane at the DA in Patient 2 were used for comparison. Fig. 6 shows comparisons of axial velocity contours extracted from the PC-MR images and the corresponding CFD simulations at different time points along the cardiac cycle. It should be noted that forward flow (from head to foot) is shown in red while backward flow is shown in blue. This comparison demonstrated good qualitative and quantitative agreements between the predicted and MR-measured velocity profiles. At mid-systolic acceleration, the flow was dominated by forward flow. At mid-systolic deceleration, the flow became more disturbed, and a region of reverse flow could be observed. This region was further extended into diastole, and flow reversal became dominant in late-diastole. Both the pre- and post-PEARS aortas followed the same flow patterns at this location.

3.3 Wall shear stress

Local WSS analysis was performed at four transverse sections (P1, P2, P3 and P4) along the aorta, as shown in Fig. 7. First, the pre- and post-PEARS WSS at the selected sections showed similar patterns, although some differences can be noted in Patient 1 but there was virtually no difference in Patient 3. In general, high WSS occurred in the systolic phase, when velocities were high. At P1, the peak WSS was found on the inner curvature of the aorta, but WSS at this location was generally lower than at the other locations. At P2, the peak WSS was still located at the inner curvature, with increases in WSS on the outer curvature of the aortic wall. At P3, the peak WSS started to shift from the inner curvature to the outer curvature under the influence of centrifugal pressure gradient (Seed and Wood, 1971); a relatively uniform distribution of WSS along the circumference of the aorta was beginning to form; this location had the highest WSS values when compared with the other planes. At P4, the distribution of WSS was more uniform along the circumference; and the magnitude of WSS was lower than the values found before and after the aortic arch.

Fig. 8 shows comparisons of circumferentially averaged WSS at peak systole at each of these planes, before and after PEARS implantation. Both Patients 2 and 3 showed increased average WSS after PEARS implantation at locations P1, P2 and P3 with little change at P4, but Patient 1 exhibited reduced WSS at all locations except at P2. Variations in WSS can be ascribed to changes in aortic diameter, local curvature and flow rate, where increased flow rate or reduced diameter (as in Patients 2 and 3, Table 2) would typically lead to an increase in WSS.

The time-averaged WSS contour plots shown in Fig. 9 revealed a similar pattern before and after PEARS implantation, with WSS in the ascending aorta being lower than in the arch and descending aorta. High TAWSS values were localised at the junctions of arch branches.

4 Discussion

MFS is a genetic disease that causes fragmentation of the elastic framework of the aortic wall, which is prone to progressive aortic dilatation resulting in a thinned aortic wall (Dormand and Mohiaddin, 2013). Aortic dilatation, particularly at the root, was a prominent morphological feature in the three cases examined in this study. Although the genetic basis of the disease is understood, it has been suggested that the biomechanical environment can contribute to the progression from aortic dilatation to aortic dissection (Dormand and Mohiaddin, 2013, Geiger et al., 2012, Geiger et al., 2013).

Lorenz et al. (2014) suggested that quantification of flow helicity combined with WSS analysis may help predict the risk for aortic aneurysm development or rupture in patients with bicuspid aortic valves. This is on the basis that helicity is influenced by the geometry of the aorta. An increase in helicity implies a higher friction between the blood flow and vessel wall, hence a higher WSS (Lorenz et al., 2014). In the present study, velocity patterns, helicity densities, instantaneous WSS maps and time-averaged WSS contours were used to make a qualitative assessment of the aortic haemodynamics before and after PEARS implantation, while HFI was adopted to quantitatively compare its helicity flow contents. It was shown that regions of low velocity and helicity densities (such as the aortic root) corresponded to low WSS while regions of high velocity and helicity densities (the aortic arch and DA) corresponded to high WSS. It is well established that WSS influences endothelial cell function, gene expression and the structure of cells, and is associated with vascular remodelling (Davies, 1995, Malek et al., 1999, Reneman et al., 2006, Levick, 2010). That is, morphological changes occur under abnormal flow conditions and are closely associated with the development of aortopathy (Geiger et al., 2013, Bieging et al., 2011, Mahadevia et al., 2014). Reduced WSS (like that observed in the aortic root) is associated with aortic dilatation.

Comparisons between the pre- and post-PEARS aortas revealed minor quantitative differences in haemodynamic parameters. Changes in haemodynamic parameters observed between the pre- and post-PEARS aortas could be ascribed to changes in aortic diameters and cardiac output. It should be noted that the primary purpose of the PEARS is to prevent further dilatation, thereby reducing the risk of aortic dissection. Based on the aortic diameters given in Table 2, Patient 1 had a slightly dilated aorta after implantation especially in the unprotected part (P3 and P4), whereas Patients 2 and 3 showed a small regression of aortic diameter. The post-PEARS MR images were acquired between one to four years after implantation, and there was no clear distinction between the aortic wall and PEARS since the device had become integrated into the outer layers of the wall, as demonstrated experimentally (Verbrugghe et al., 2013, Pepper et al., 2014). It can therefore be hypothesised that morphological and functional alterations of the aortic wall in the post-PEARS aorta resulted in the observed changes in the haemodynamic parameters when compared with the pre-PEARS aorta.

The current study has a number of limitations. First, the aortic wall was assumed to be rigid with no translational motion or radial expansion. Since the portion of ascending aorta wrapped in the PEARS is much stiffer than the native aorta (Singh et al., 2015), this assumption is likely to cause underestimation of the differences in flow patterns and WSS between pre- and post-PEARS aortas. Second, in the absence of patient-specific measurement of flow through the arch branches, a total of 30% aortic flow was assumed to leave through the branches, based on PC-MRI data acquired from human aortas in a separate study (Cheng et al., 2015). The validity of this assumption was tested through a sensitivity analysis with flow partitions of 30.0±7.2% to the arch vessels, details of which can be found in Appendix A3. It is also worth noting that the amount of flow entering the arch branches is influenced by many factors, including brain activity, resistance in the downstream vasculature and upper body movement. Since the present study is focused on comparing flow in the main aorta before and after implantation of PEARS, applying a fixed flow partition in all simulations is not an unreasonable assumption in the absence of patient-specific flow partitions. Finally, although patient-specific inflow conditions were obtained from PC-MRI, flow at the inlet was assumed to be in the axial direction only. The exclusion of secondary velocity components at the inlet is likely to affect the accuracy in reproducing the vertical flow structure in the aorta (Morbiducci et al., 2013). Nevertheless, despite these limitations, comparisons between MR-derived and computed velocity profiles for Patient 2 revealed a good agreement, both qualitatively and quantitatively.

5 Conclusion

In this study, a detailed assessment of the flow patterns and WSS in the Marfan aorta was performed in three patients who underwent implantation of PEARS. Flow simulations were performed based on patient-specific geometries and MR-derived boundary conditions (pre- and post-PEARS). Velocity patterns, helicity densities, $\overline{\mathrm{HFI}}$ and WSS were used to analyse the haemodynamic implications of PEARS. The results showed that qualitative distributions of the haemodynamic parameters in the pre- and post-PEARS aortas were similar while quantitative measures showed small variations, which may be attributed to geometrical and functional changes of the composite aortic wall. Future studies including a larger cohort of patients are required to assess the statistical significance and clinical relevance of the findings.

6 Acknowledgements

The first author is supported by a PhD scholarship from the government of the Republic of Trinidad and Tobago. Dr Zhuo Cheng of Imperial College London helped with the evaluation of helical flow indices.

7 Conflicts of interest

None.

References

AHMED, S. A. & GIDDENS, D. P. 1983a. Flow disturbance measurements through a constricted tube at moderate Reynolds numbers. *J Biomech,* 16**,** 955-63.

AHMED, S. A. & GIDDENS, D. P. 1983b. Velocity measurements in steady flow through axisymmetric stenoses at moderate Reynolds numbers. *J Biomech,* 16**,** 505-16.

BARKER, A. J., LANNING, C. & SHANDAS, R. 2010. Quantification of hemodynamic wall shear stress in patients with bicuspid aortic valve using phase-contrast MRI. *Ann Biomed Eng,* 38**,** 788-800.

BARTH, T. & JESPERSEN, D. 1989. The design and application of upwind schemes on unstructured meshes. *27th Aerospace Sciences Meeting.* American Institute of Aeronautics and Astronautics.

BELLHOUSE, B. J. & TALBOT, L. 1969. The fluid mechanics of the aortic valve. *Journal of Fluid Mechanics,* 35**,** 721-735.

BENTALL, H. & DE BONO, A. 1968. A technique for complete replacement of the ascending aorta. *Thorax,* 23**,** 338-339.

BIEGING, E. T., FRYDRYCHOWICZ, A., WENTLAND, A., LANDGRAF, B. R., JOHNSON, K. M., WIEBEN, O. & FRANCOIS, C. J. 2011. In vivo three-dimensional MR wall shear stress estimation in ascending aortic dilatation. *J Magn Reson Imaging,* 33**,** 589-97.

BOGREN, H. G. & BUONOCORE, M. H. 1999. 4D magnetic resonance velocity mapping of blood flow patterns in the aorta in young vs. elderly normal subjects. *J Magn Reson Imaging,* 10**,** 861-9.

CHENG, Z., WOOD, N. B., GIBBS, R. G. & XU, X. Y. 2015. Geometric and flow features of type B aortic dissection: initial findings and comparison of medically treated and stented cases. *Ann Biomed Eng,* 43**,** 177-89.

DAVID, T. E., FEINDEL, C. M. & BOS, J. 1995. Repair of the aortic valve in patients with aortic insufficiency and aortic root aneurysm. *The Journal of Thoracic and Cardiovascular Surgery,* 109**,** 345-352.

DAVIES, P. F. 1995. Flow-mediated endothelial mechanotransduction. *Physiol Rev,* 75**,** 519-60.

DORMAND, H. & MOHIADDIN, R. H. 2013. Cardiovascular magnetic resonance in Marfan syndrome. *J Cardiovasc Magn Reson,* 15**,** 33.

FERZIGER, J. H. & PERIC, M. 2001. *Computational Methods for Fluid Dynamics,* Springer Berlin Heidelberg.

GEIGER, J., ARNOLD, R., HERZER, L., HIRTLER, D., STANKOVIC, Z., RUSSE, M., LANGER, M. & MARKL, M. 2013. Aortic wall shear stress in Marfan syndrome. *Magn Reson Med,* 70, 1137-44.

GEIGER, J., MARKL, M., HERZER, L., HIRTLER, D., LOEFFELBEIN, F., STILLER, B., LANGER, M. & ARNOLD, R. 2012. Aortic flow patterns in patients with Marfan syndrome assessed by flow-sensitive four-dimensional MRI. *J Magn Reson Imaging,* 35, 594-600.

GOLESWORTHY, T., LAMPERTH, M., MOHIADDIN, R., PEPPER, J., THORNTON, W. & TREASURE, T. 2004. The Tailor of Gloucester: a jacket for the Marfan's aorta. *Lancet,* 364, 1582.

GRIGIONI, M., DANIELE, C., MORBIDUCCI, U., DEL GAUDIO, C., D'AVENIO, G., BALDUCCI, A. & BARBARO, V. 2005. A mathematical description of blood spiral flow in vessels: application to a numerical study of flow in arterial bending. *J Biomech,* 38, 1375-86.

HESS, P. J., JR., KLODELL, C. T., BEAVER, T. M. & MARTIN, T. D. 2005. The Florida sleeve: a new technique for aortic root remodeling with preservation of the aortic valve and sinuses. *Ann Thorac Surg,* 80, 748-50.

HOPE, M. D., HOPE, T. A., MEADOWS, A. K., ORDOVAS, K. G., URBANIA, T. H., ALLEY, M. T. & HIGGINS, C. B. 2010. Bicuspid Aortic Valve: Four-dimensional MR Evaluation of Ascending Aortic Systolic Flow Patterns. *Radiology,* 255, 53-61.

JUDGE, D. P. & DIETZ, H. C. 2005. Marfan's syndrome. *The Lancet,* 366, 1965-1976.

KILNER, P. J., YANG, G. Z., MOHIADDIN, R. H., FIRMIN, D. N. & LONGMORE, D. B. 1993. Helical and retrograde secondary flow patterns in the aortic arch studied by three-directional magnetic resonance velocity mapping. *Circulation,* 88, 2235-47.

KOUSERA, C. A., WOOD, N. B., SEED, W. A., TORII, R., O'REGAN, D. & XU, X. Y. 2013. A Numerical Study of Aortic Flow Stability and Comparison With In Vivo Flow Measurements. *Journal of Biomechanical Engineering-Transactions of the Asme,* 135.

LANGTRY, R. B. & MENTER, F. R. 2009. Correlation-Based Transition Modeling for Unstructured Parallelized Computational Fluid Dynamics Codes. *AIAA Journal*, 47, 2894-2906.

LANTZ, J., EBBERS, T., ENGVALL, J. & KARLSSON, M. 2013. Numerical and experimental assessment of turbulent kinetic energy in an aortic coarctation. *J Biomech,* 46, 1851-8.

LANTZ, J., GARDHAGEN, R. & KARLSSON, M. 2012. Quantifying turbulent wall shear stress in a subject specific human aorta using large eddy simulation. *Med Eng Phys,* 34, 1139-48..

LANTZ, J., RENNER, J. & KARLSSON, M. 2011. Wall shear stress in a subject specific human aorta - Influence of fluid-structure interation. *International Journal of Applied Mechanics*, 03, 759-778.

LEVICK, J. R. 2010. *An introduction to cardiovascular physiology,* London, Hodder Arnold.

LORENZ, R., BOCK, J., BARKER, A. J., VON KNOBELSDORFF-BRENKENHOFF, F., WALLIS, W., KORVINK, J. G., BISSELL, M. M., SCHULZ-MENGER, J. & MARKL, M. 2014. 4D flow magnetic resonance imaging in bicuspid aortic valve disease demonstrates altered distribution of aortic blood flow helicity. *Magn Reson Med,* 71, 1542-53.

MAHADEVIA, R., BARKER, A. J., SCHNELL, S., ENTEZARI, P., KANSAL, P., FEDAK, P. W., MALAISRIE, S. C., MCCARTHY, P., COLLINS, J., CARR, J. & MARKL, M. 2014. Bicuspid aortic cusp fusion morphology alters aortic three-dimensional outflow patterns, wall shear stress, and expression of aortopathy. *Circulation,* 129, 673-82.

MALEK, A. M., ALPER, S. L. & IZUMO, S. 1999. Hemodynamic shear stress and its role in atherosclerosis. *JAMA,* 282, 2035-42.

MARKL, M., GEIGER, J., HERZER, L., STILLER, B. & ARNOLD, R. 2011a. 3D Aortic Blood Flow in Patients with Marfan Syndrome: Changes in Hemodynamics and Correlation with Aortic Geometry. *Proc. Intl. Soc.Mag. Reson. Med,* 19.

MARKL, M., KILNER, P. J. & EBBERS, T. 2011b. Comprehensive 4D velocity mapping of the heart and great vessels by cardiovascular magnetic resonance. *J Cardiovasc Magn Reson,* 13, 7.

MENTER, F. R. 1994. 2-Equation Eddy-Viscosity Turbulence Models for Engineering Applications. *Aiaa Journal,* 32, 1598-1605.

MITTAL, R., SIMMONS, S. P. & NAJJAR, F. 2003. Numerical study of pulsatile flow in a constricted channel. *Journal of Fluid Mechanics,* 485, 337-378.

MORBIDUCCI, U., PONZINI, R., GALLO, D., BIGNARDI, C. & RIZZO, G. 2013. Inflow boundary conditions for image-based computational hemodynamics: impact of idealized versus measured velocity profiles in the human aorta. *J Biomech,* 46, 102-9.

MORBIDUCCI, U., PONZINI, R., RIZZO, G., CADIOLI, M., ESPOSITO, A., DE COBELLI, F., DEL MASCHIO, A., MONTEVECCHI, F. M. & REDAELLI, A. 2009. In vivo quantification of helical blood flow in human aorta by time-resolved three-dimensional cine phase contrast magnetic resonance imaging. *Ann Biomed Eng,* 37, 516-31.

MORBIDUCCI, U., PONZINI, R., RIZZO, G., CADIOLI, M., ESPOSITO, A., MONTEVECCHI, F. M. & REDAELLI, A. 2011. Mechanistic insight into the physiological relevance of helical blood flow in the human aorta: an in vivo study. *Biomech Model Mechanobiol,* 10, 339-55.

OLUFSEN, M. S., PESKIN, C. S., KIM, W. Y., PEDERSEN, E. M., NADIM, A. & LARSEN, J. 2000. Numerical simulation and experimental validation of blood flow in arteries with structured-tree outflow conditions. *Ann Biomed Eng,* 28, 1281-99.

PAUL, M. C., MAMUN MOLLA, M. & RODITI, G. 2009. Large-Eddy simulation of pulsatile blood flow. *Med Eng Phys,* 31, 153-9.

PEPPER, J., GODDARD, M., MOHIADDIN, R. & TREASURE, T. 2014. Histology of a Marfan aorta 4.5 years after personalized external aortic root support. *Eur J Cardiothorac Surg,* 48, 502-5.

PEPPER, J., JOHN CHAN, K., GAVINO, J., GOLESWORTHY, T., MOHIADDIN, R. & TREASURE, T. 2010. External aortic root support for Marfan syndrome: early clinical results in the first 20 recipients with a bespoke implant. *J R Soc Med,* 103, 370-5.

RENEMAN, R. S., ARTS, T. & HOEKS, A. P. 2006. Wall shear stress--an important determinant of endothelial cell function and structure--in the arterial system in vivo. Discrepancies with theory. *J Vasc Res,* 43, 251-69.

SEED, W. A. & WOOD, N. B. 1971. Velocity patterns in the aorta. *Cardiovasc Res,* 5, 319-30.

SILVERMAN, D. I., GRAY, J., ROMAN, M. J., BRIDGES, A., BURTON, K., BOXER, M., DEVEREUX, R. B. & TSIPOURAS, P. 1995. Family history of severe cardiovascular disease in Marfan syndrome is associated with increased aortic diameter and decreased survival. *J Am Coll Cardiol,* 26, 1062-7.

SINGH, S. D., XU, X. Y., PEPPER, J. R., TREASURE, T. & MOHIADDIN, R. H. 2015. Biomechanical properties of the Marfan's aortic root and ascending aorta before and after personalised external aortic root support surgery. *Med Eng Phys,* 37, 759-66.

STALDER, A. F., FRYDRYCHOWICZ, A., RUSSE, M. F., KORVINK, J. G., HENNIG, J., LI, K. & MARKL, M. 2011. Assessment of flow instabilities in the healthy aorta using flow-sensitive MRI. *J Magn Reson Imaging,* 33, 839-46.

STEIN, P. D. & SABBAH, H. N. 1976. Turbulent blood flow in the ascending aorta of humans with normal and diseased aortic valves. *Circ Res,* 39, 58-65.

TAN, F. P., SOLOPERTO, G., BASHFORD, S., WOOD, N. B., THOM, S., HUGHES, A. & XU, X. Y. 2008. Analysis of flow disturbance in a stenosed carotid artery bifurcation using two-equation transitional and turbulence models. *J Biomech Eng,* 130, 061008.

TAN, F. P., WOOD, N. B., TABOR, G. & XU, X. Y. 2011. Comparison of LES of steady transitional flow in an idealized stenosed axisymmetric artery model with a RANS transitional model. *J Biomech Eng,* 133, 051001.

TAN, F. P. P., BORGHI, A., MOHIADDIN, R. H., WOOD, N. B., THOM, S. & XU, X. Y. 2009a. Analysis of flow patterns in a patient-specific thoracic aortic aneurysm model. *Computers & Structures,* 87, 680-690.

TAN, F. P. P., TORII, R., BORGHI, A., MOHIADDIN, R. H., WOOD, N. B. & XU, X. Y. 2009b. Fluid-Structure Interaction Analysis of Wall Stress and Flow Patterns in a Thoracic Aortic Aneurysm. *International Journal of Applied Mechanics,* 1, 179-199.

TAN, F. P. P., XU, X. Y., TORII, R., WOOD, N. B., DELAHUNTY, N., MULLEN, M., MOAT, N. & MOHIADDIN, R. 2012. Comparison of Aortic Flow Patterns Before and After Transcatheter Aortic Valve Implantation. *Cardiovascular Engineering and Technology,* 3, 123-135.

TREASURE, T., TAKKENBERG, J. J. & PEPPER, J. 2014. Surgical management of aortic root disease in Marfan syndrome and other congenital disorders associated with aortic root aneurysms. *Heart*.

VARGHESE, S. S., FRANKEL, S. H. & FISCHER, P. F. 2007a. Direct numerical simulation of stenotic flows. Part 1. Steady flow. *Journal of Fluid Mechanics*, 582**,** 253-280.

VARGHESE, S. S., FRANKEL, S. H. & FISCHER, P. F. 2007b. Direct numerical simulation of stenotic flows. Part 2. Pulsatile flow. *Journal of Fluid Mechanics,* 582**,** 281-318.

VARGHESE, S. S., FRANKEL, S. H. & FISCHER, P. F. 2008. Modeling transition to turbulence in eccentric stenotic flows. *J Biomech Eng,* 130**,** 014503.

VERBRUGGHE, P., VERBEKEN, E., PEPPER, J., TREASURE, T., MEYNS, B., MEURIS, B., HERIJGERS, P. & REGA, F. 2013. External aortic root support: a histological and mechanical study in sheep. *Interact Cardiovasc Thorac Surg,* 17**,** 334-9.

WENDELL, D. C., SAMYN, M. M., CAVA, J. R., ELLWEIN, L. M., KROLIKOWSKI, M. M., GANDY, K. L., PELECH, A. N., SHADDEN, S. C. & LADISA, J. F., JR. 2013. Including aortic valve morphology in computational fluid dynamics simulations: initial findings and application to aortic coarctation. *Med Eng Phys,* 35**,** 723-35.

YACOUB, M. H., GEHLE, P., CHANDRASEKARAN, V., BIRKS, E. J., CHILD, A. & RADLEY-SMITH, R. 1998. Late results of a valve-preserving operation in patients with aneurysms of the ascending aorta and root. *J Thorac Cardiovasc Surg,* 115**,** 1080-90.

Fig. 1. Magnetic resonance imaging of the aorta and implantation of PEARS.

Fig. 2. (a) Patient-specific aortic geometries reconstructed from pre-PEARS and post-PEARS MR images for Patient 1 (top), Patient 2 (middle) and Patient 3 (bottom); (b) Corresponding flow waveforms extracted from PC-MR images.

Fig. 3. Comparison of pre- and post-PEARS instantaneous velocity streamlines at (a) peak systole (T_{sys}) and (b) mid-systolic deceleration (T_{mid}) for Patients 1, 2 and 3.

Fig. 4. Comparison of pre- and post-PEARS helicity density (H_k) isosurfaces at peak systole (T_{sys}) and mid-deceleration (T_{mid}) for Patients 1, 2 and 3. Red represents clockwise rotation while blue represents anti-clockwise rotation.

Fig. 5. Helicity flow indices (HFI) calculated over particle trace sets emitted at five time points T_j during systole (and over the time interval $T_{es} – T_j$) (■ Pre-PEARS; □ Post-PEARS)

Fig. 6. Comparison of axial velocity contours at different time points along the cardiac cycle between the simulation results and MR velocity data (in m/s) for Patient 2 (top: pre-PEARS, bottom: post-PEARS)

Fig. 7. Temporal WSS maps obtained at four cross-sectional planes along the aorta over the entire cardiac cycle, for Patients 1, 2 and 3. Each plane is unwrapped, with the starting (and ending) point corresponding to the inner wall of the aorta at position 0 (and 1). Distance along the circumference is measured with reference to the starting point, and normalised for comparison.

Fig. 8. Circumferential averaged WSS at peak systole at different locations (P1, P2, P3 and P4) along the aorta in Patients 1, 2 and 3 (■ Pre-PEARS; □ Post-PEARS)

Fig. 9. Time-averaged wall shear stress (TAWSS) contours in Patients 1, 2 and 3 (a, b and c) in the pre-PEARS and post-PEARS aortas (i and ii), respectively. (For each pair of TAWSS contours, left figure: left-oblique view; right figure: right-oblique view).

Table 1: Summary of patient data

	Patient 1		Patient 2		Patient 3	
Age at Pre-PEARS imaging	38		20		48	
Age at Post-PEARS imaging	42		24		49	
Sex	M		F		M	
	Pre	Post	Pre	Post	Pre	Post
BMI	21.97	21.39	26.23	23.46	23.77	24.07
Blood Pressure (mmHg)						
Systolic	135	130	110	110	118	110
Diastolic	78	70	60	60	84	70
Pulse	57	60	50	50	34	40
Cardiac output (L/min)	6.0	6.3	6.4	6.9	5.3	6.1
Peak Reynolds number	5304	6324	4502	4443	4944	4459
Mean Reynolds number	1546	1397	1174	1090	1131	1158
Womersley number	13.6	16.0	20.2	22.6	16.7	18.7

Table 2: Comparison of pre- and post-PEARS diameters (mm) along four transverse planes of the aorta

	Patient 1		Patient 2		Patient 3	
	Pre	Post	Pre	Post	Pre	Post
P1	33.1	32.1	38.8	37.3	38.7	37.5
P2	19.6	22.8	29.4	26.2	28.7	26.7
P3	20.7	24.0	24.0	22.9	22.3	20.8
P4	17.0	20.4	19.5	20.0	22.9	21.2

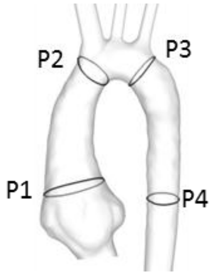

Figures
Click here to download Figure: Figures All.pdf

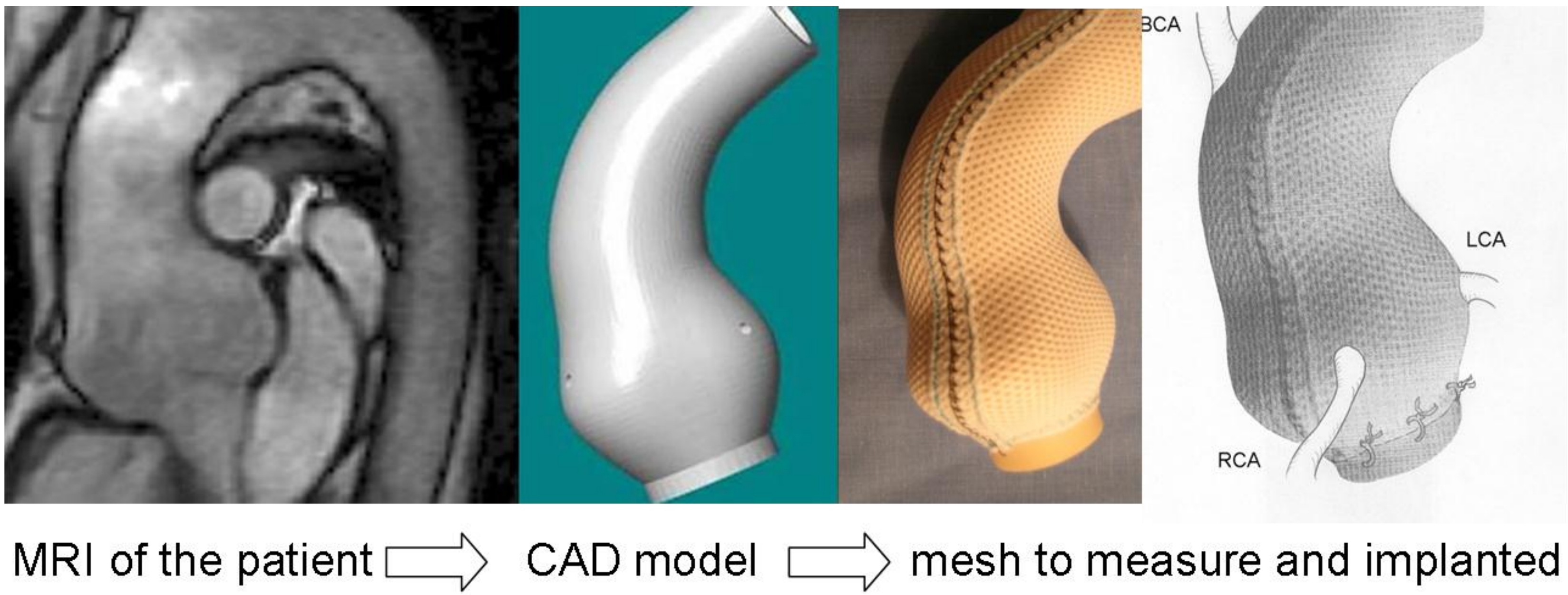

Figure 1

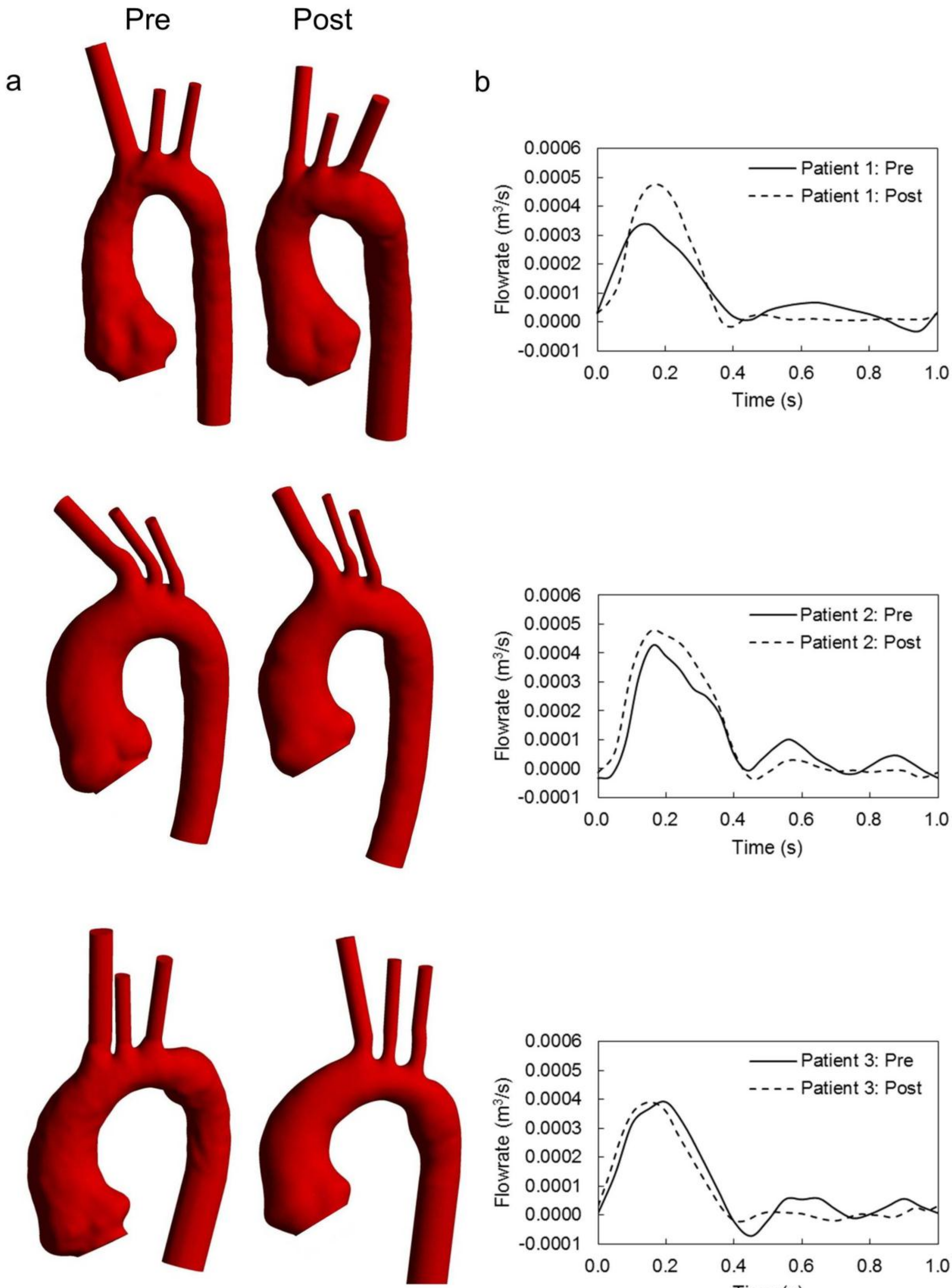
Pre
Post
a
b
Patient 1: Pre
Patient 1: Post
Patient 2: Pre
Patient 2: Post
Patient 3: Pre
Patient 3: Post
Flowrate (m³/s)
Time (s)
0.0006
0.0005
0.0004
0.0003
0.0002
0.0001
0.0000
-0.0001
0.0
0.2
0.4
0.6
0.8
1.0

Figure 2

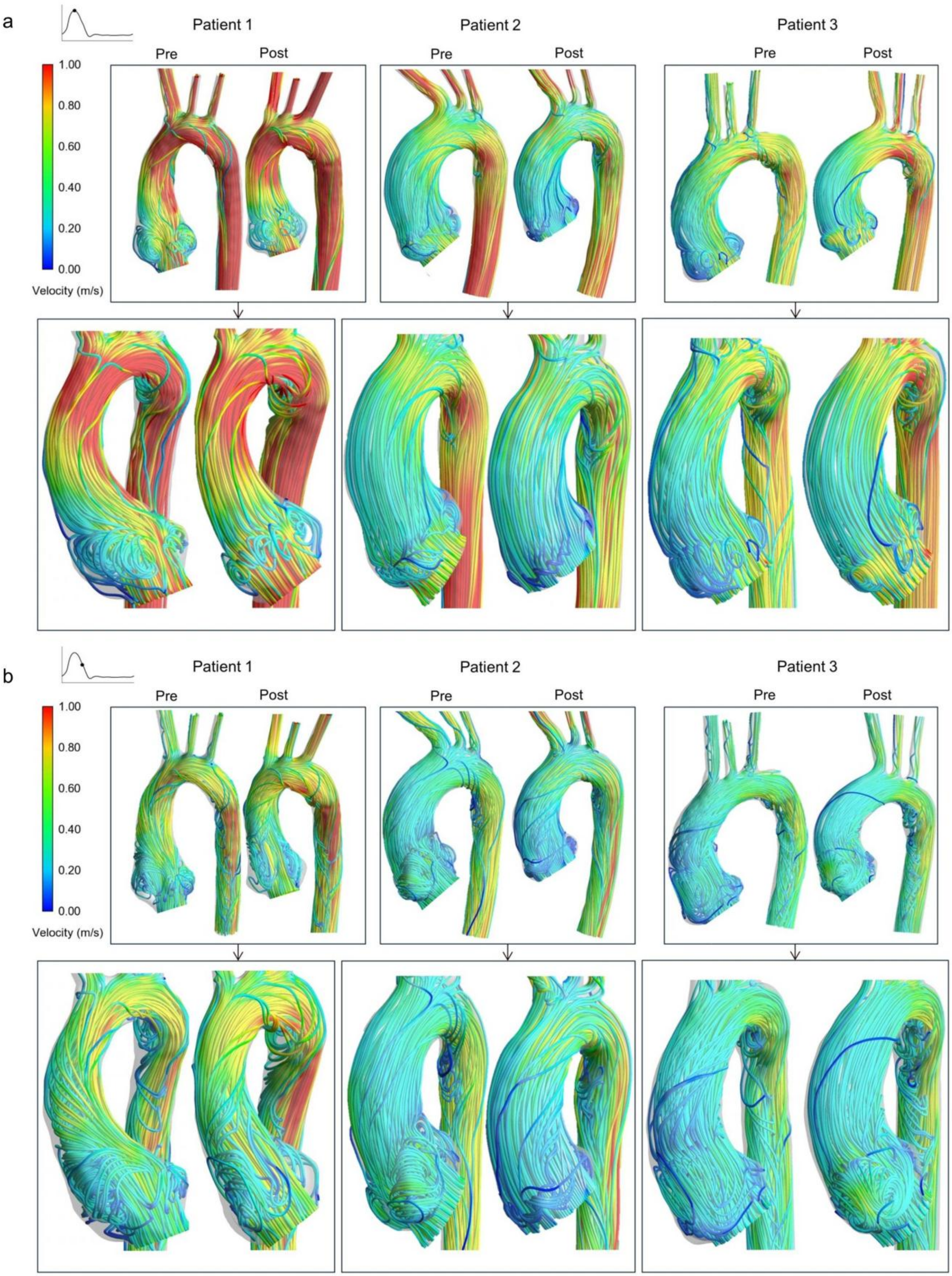
a
Patient 1
Patient 2
Patient 3
Pre
Post
Pre
Post
Pre
Post
1.00
0.80
0.60
0.40
0.20
0.00
Velocity (m/s)
b
Patient 1
Patient 2
Patient 3
Pre
Post
Pre
Post
Pre
Post
1.00
0.80
0.60
0.40
0.20
0.00
Velocity (m/s)

Figure 3

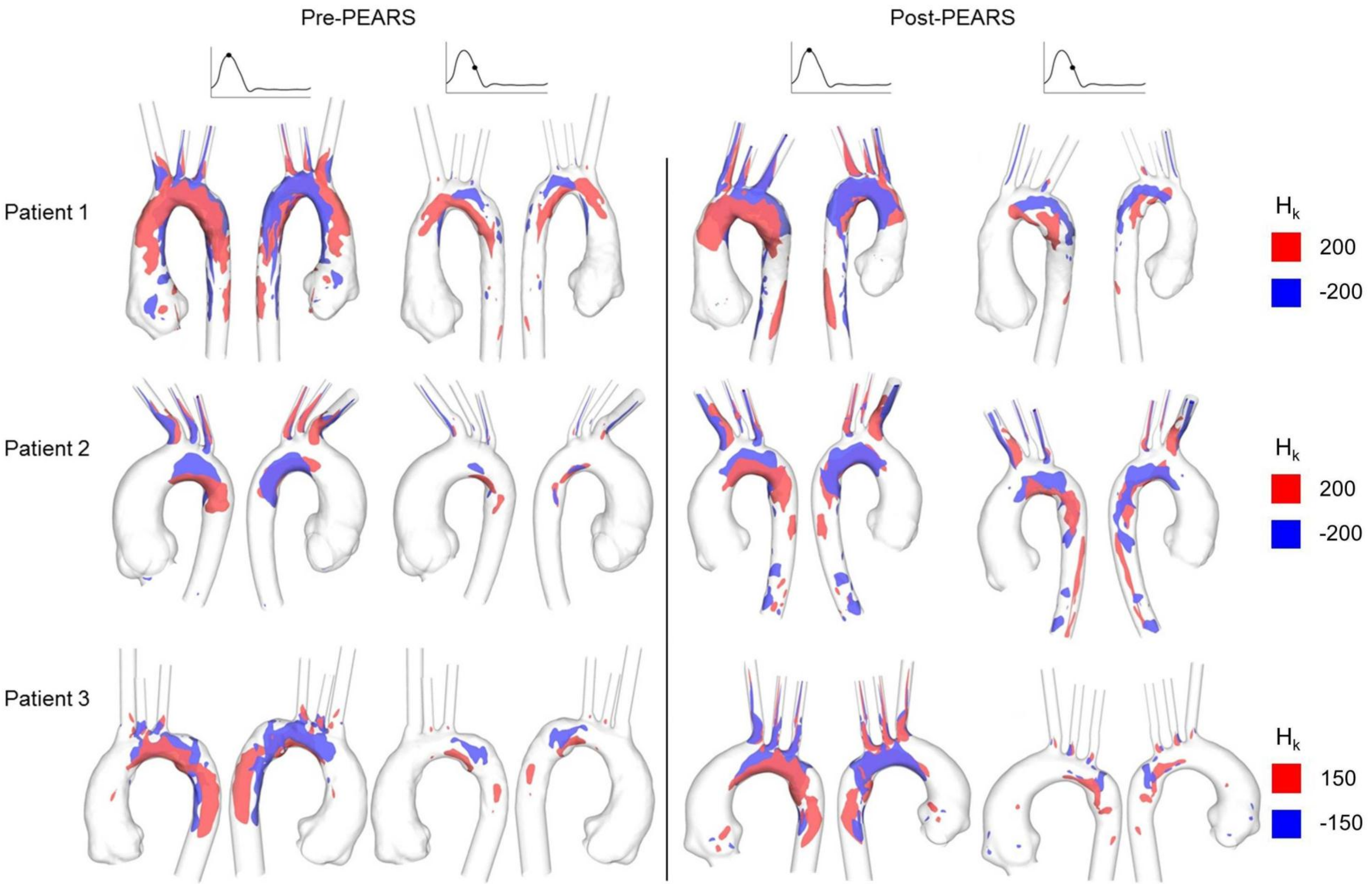
Pre-PEARS
Post-PEARS
Patient 1
Patient 2
Patient 3
H_k
200
-200
H_k
200
-200
H_k
150
-150

Figure 4

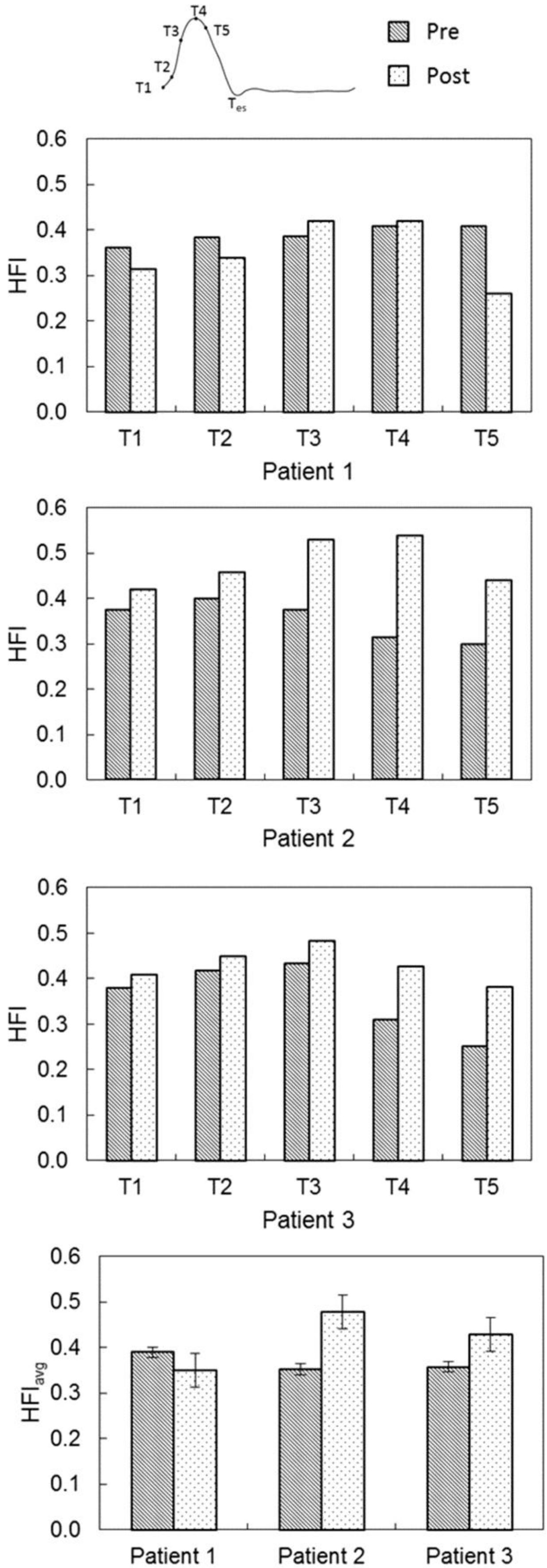
T1
T2
T3
T4
T5
Tes
Pre
Post
0.6
0.5
0.4
0.3
0.2
0.1
0.0
HFI
T1 T2 T3 T4 T5
Patient 1
Patient 2
Patient 3
HFIavg
Patient 1 Patient 2 Patient 3

Figure 5

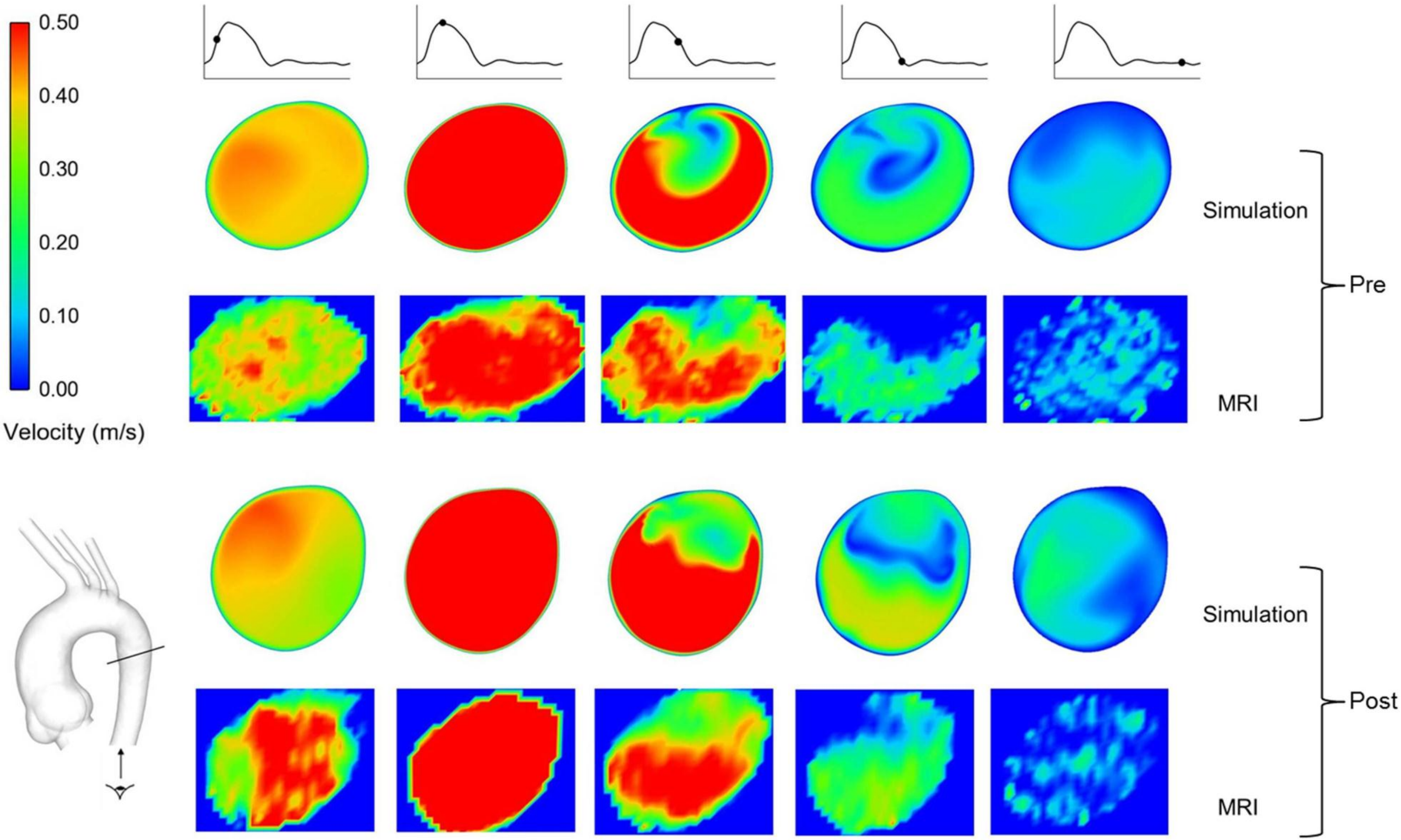

0.50
0.40
0.30
0.20
0.10
0.00
Velocity (m/s)
Simulation
MRI
Pre
Simulation
MRI
Post

Figure 6

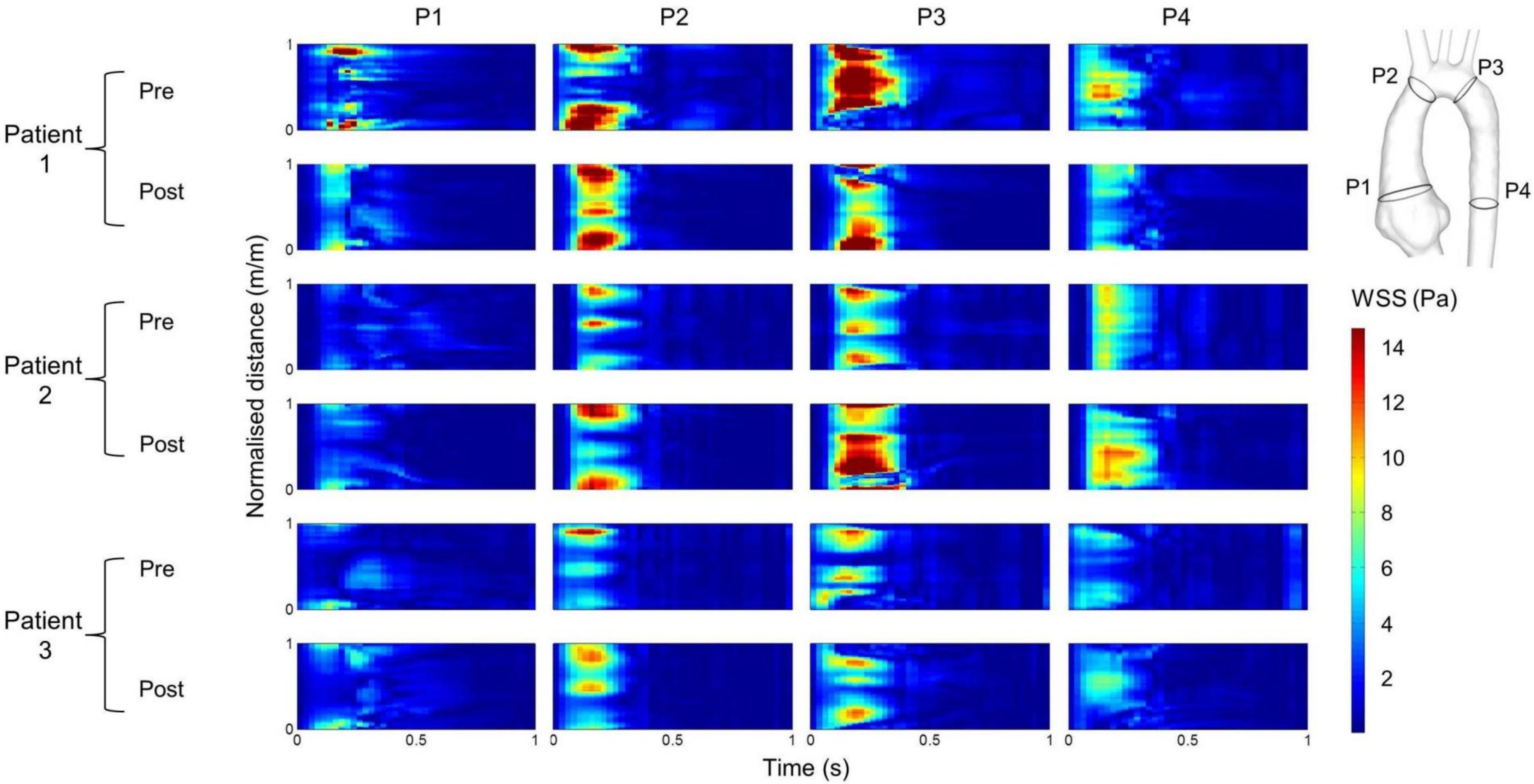
P1
P2
P3
P4
Patient 1
Pre
Post
Patient 2
Pre
Post
Patient 3
Pre
Post
Normalised distance (m/m)
Time (s)
WSS (Pa)
14
12
10
8
6
4
2
0
0.5
1

Figure 7

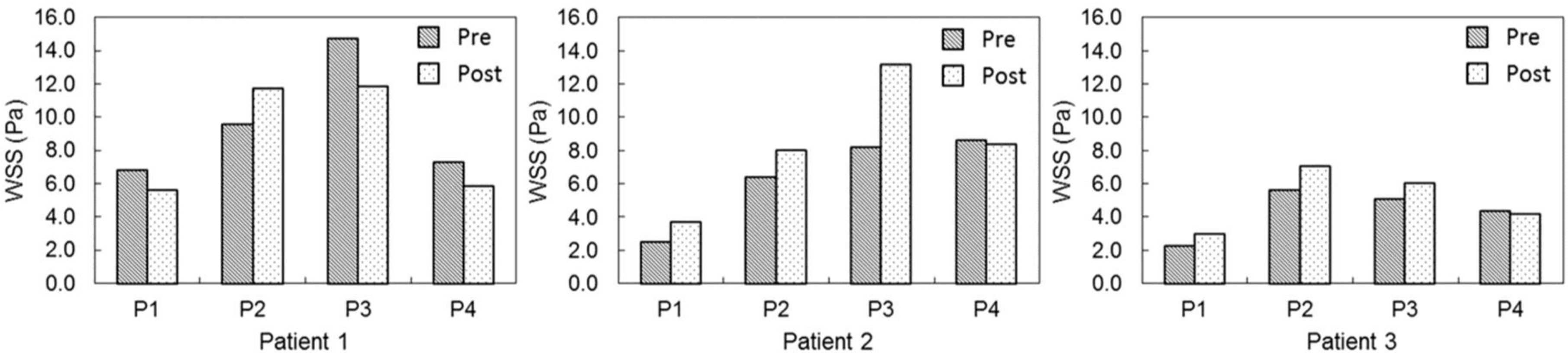

16.0
14.0
12.0
10.0
8.0
6.0
4.0
2.0
0.0
WSS (Pa)
Pre
Post
P1
P2
P3
P4
Patient 1
Patient 2
Patient 3

Figure 8

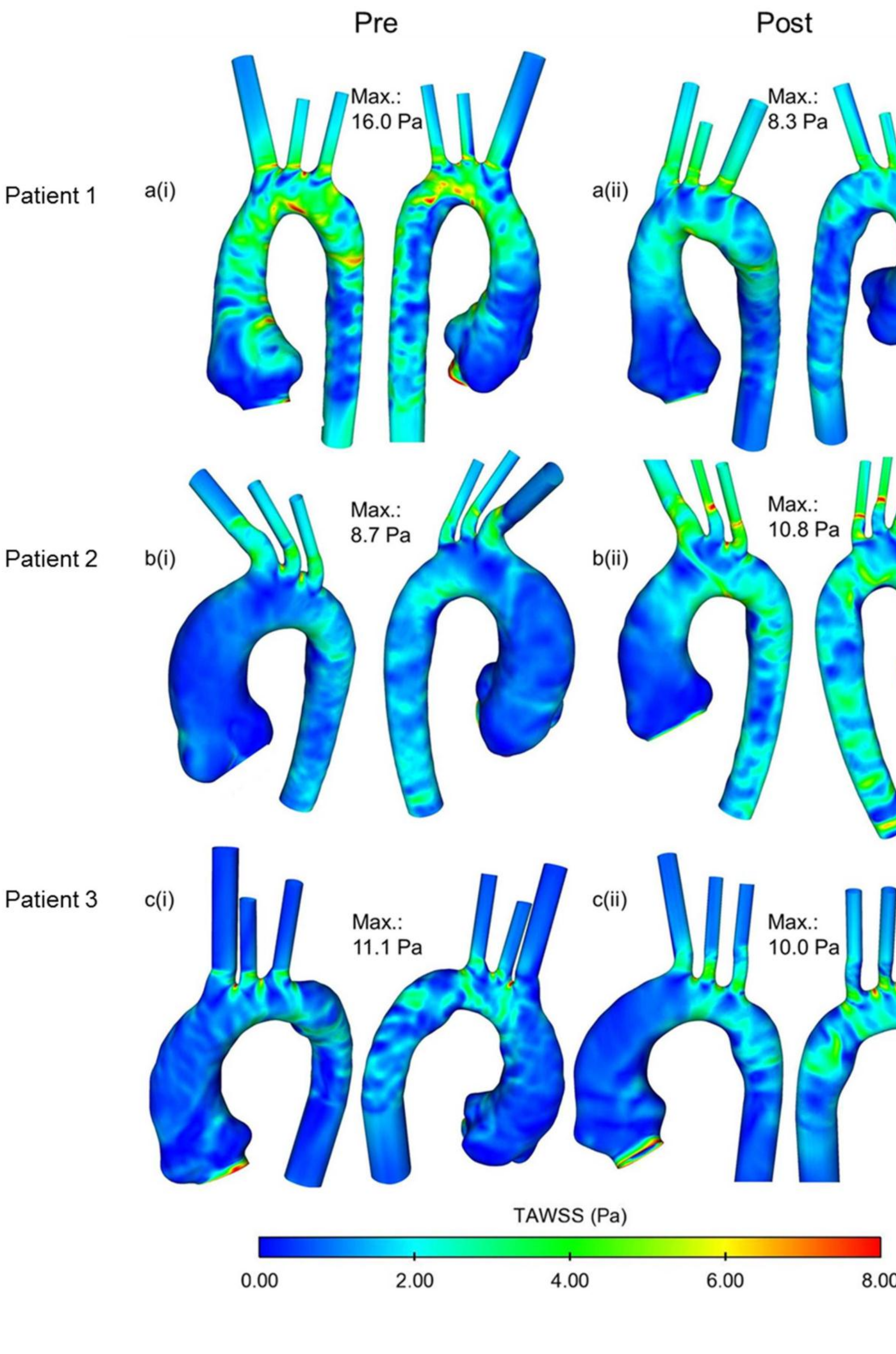

Pre
Post
Patient 1
a(i)
Max.:
16.0 Pa
a(ii)
Max.:
8.3 Pa
Patient 2
b(i)
Max.:
8.7 Pa
b(ii)
Max.:
10.8 Pa
Patient 3
c(i)
Max.:
11.1 Pa
c(ii)
Max.:
10.0 Pa
TAWSS (Pa)
0.00
2.00
4.00
6.00
8.00

Figure 9